# Absence of topological Hall effect in $Fe_xRh_{100-x}$ epitaxial films: Revisiting their phase diagram

Xiaoyan Zhu,[1] Hui Li,[2] Jing Meng,[1] Xinwei Feng,[1] Zhixuan Zhen,[1] Haoyu Lin,[1] Bocheng Yu,[1] Wenjuan Cheng,[1] Dongmei Jiang,[1] Yang Xu,[1] Tian Shang,[1,3,*] and Qingfeng Zhan[1,†]

[1]*Key Laboratory of Polar Materials and Devices (MOE), School of Physics and Electronic Science, East China Normal University, Shanghai 200241, China*

[2]*Cavendish Laboratory, University of Cambridge, J J Thomson Avenue, Cambridge CB3 0HE, United Kingdom*

[3]*Chongqing Key Laboratory of Precision Optics, Chongqing Institute of East China Normal University, Chongqing 401120, China*

(Received 15 May 2023; accepted 10 October 2023; published 26 October 2023)

A series of $Fe_xRh_{100-x}$ ($30 \leqslant x \leqslant 57$) films were epitaxially grown using magnetron sputtering, and were systematically studied by magnetization, electrical resistivity, and Hall resistivity measurements. After optimizing the growth conditions, phase-pure $Fe_xRh_{100-x}$ films were obtained, and their magnetic phase diagram was revisited. The ferromagnetic (FM) to antiferromagnetic (AFM) transition is limited at narrow Fe contents with $48 \leqslant x \leqslant 54$ in the bulk $Fe_xRh_{100-x}$ alloys. By contrast, the FM-AFM transition in the $Fe_xRh_{100-x}$ films is extended to cover a much wider $x$ range between 33% and 53%, whose critical temperature slightly decreases with increasing Fe content. The resistivity jump and magnetization drop at the FM-AFM transition are much more significant in the $Fe_xRh_{100-x}$ films with ∼50% Fe content than in the Fe-deficient films; the latter have a large amount of paramagnetic phase. The magnetoresistivity (MR) is rather weak and positive in the AFM state, while it becomes negative when the FM phase shows up, and a giant MR appears in the mixed FM and AFM state. The Hall resistivity is dominated by the ordinary Hall effect in the AFM state, while in the mixed state or high-temperature FM state, the anomalous Hall effect takes over. The absence of topological Hall resistivity in $Fe_xRh_{100-x}$ films with various Fe contents implies that the previously observed topological Hall effect is most likely extrinsic. We propose that the anomalous Hall effect caused by the FM iron moments at the interfaces nicely explains the hump-like anomaly in the Hall resistivity data. Our systematic investigations may offer valuable insights into the spintronics based on iron-rhodium alloys.

DOI: 10.1103/PhysRevB.108.144437

## I. INTRODUCTION

The CsCl-ordered equiatomic iron-rhodium (Fe-Rh) alloy undergoes a first-order magnetic phase transition from the high-temperature ferromagnetic (FM) state to the low-temperature antiferromagentic (AFM) state near room temperature [1,2]. Such a transition leads to a significant drop in the magnetization and a jump in the electrical resistivity, which can be applied to the spintronic devices. The FM-AFM transition in Fe-Rh alloys can be easily tuned by external control parameters, such as chemical substitution [3], epitaxial strain [4–6], and magnetic or electric fields [7–10]. Many exotic properties that are closely related to their FM-AFM transition have been found in Fe-Rh alloys. The spin-orbit torque efficiency can be significantly tuned by varying the temperature across the FM-AFM transition in Fe-Rh-based heterostructures [11]. The large magnetocaloric effect can be controlled by ferroelectric domains in Fe-Rh film near the FM-AFM transition [12]. Since the FM-AFM transition presents near the room temperature, therefore, Fe-Rh alloys represent one of the ideal candidate materials for spintronic applications, such as memory resistor [13], heat-assisted magnetic recording [14], and magnetic refrigeration [12].

The bulk Fe-Rh alloys exhibit a rich phase diagram when varying the Fe or Rh concentrations. We summarize the phase diagram of bulk Fe-Rh alloys in Fig. 1(a). On the Rh-rich side, the $\gamma$-PM indicates the paramagnetic (PM) phase with a face-centered cubic (FCC) crystal structure, where both Rh and Fe atoms occupy the same sites [see Fig. 1(b)]. For the intermediate Fe concentration (<48%), the Fe-Rh alloys adopt the mixed $\alpha$ and $\gamma$ phases. While the $\gamma$ phase remains PM, the $\alpha$ phase becomes FM below certain temperatures [denoted as ($\alpha$+$\gamma$)-(FM+PM) in Fig. 1(a)]. When increasing the Fe content above 48%, the Fe-Rh alloys show a pure $\alpha$ phase with a body-centered cubic (BCC) crystal structure. In particular, the Fe-Rh alloys with 48-54% Fe content undergo multiple magnetic transitions, from high-temperature PM state (marked as $\alpha$-PM) to the FM state ($\alpha$-FM), and then finally to the low-temperature AFM state ($\alpha$-AFM). The FM-AFM transition temperature decreases as increasing the Fe content. For these alloys, the Fe and Rh atoms occupy the corner and center sites, respectively [see Fig. 1(c)]. It is noted that the $\alpha$-FM and $\alpha$-AFM are also known as ordered $\alpha$' phase and $\alpha$" phase. On the Fe-rich side, both Rh and Fe atoms occupy the same sites [see Fig. 1(d)], and the Fe-Rh alloys behave similarly to a pure Fe metal, exhibiting a FM ground state below the Curie temperature (∼1000 K). In the $\alpha$-AFM

*tshang@phy.ecnu.edu.cn
†qfzhan@phy.ecnu.edu.cn

 

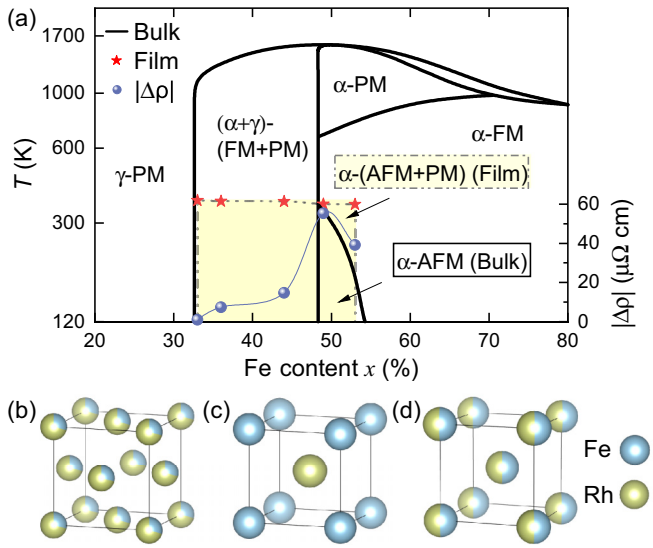


FIG. 1. (a) Phase diagram of bulk Fe-Rh alloys and epitaxial Fe-Rh films. Data of bulk alloys were taken from Refs. [16,27]. The star symbols represent the FM-AFM magnetic transition temperatures (left axis) for Fe-Rh films, while the sphere symbols show the resistivity jump $|\Delta\rho|$ (right axis) for these films against the Fe content. Crystal structures for (b) $\gamma$ phase (FCC, $Fm$-3$m$, No. 225) and (c) $\alpha$ phase (BCC, $Pm$-3$m$, No. 221) Fe-Rh. The crystal structure of disordered $\alpha$ phase is shown in panel (d). Different from the ordered $\alpha$ phase in (c), the Fe or Rh atoms occupy the same site in the disordered $\alpha$ phase and $\gamma$ phase.

phase, the Fe moments are aligned with a collinear G-type magnetic structure, exhibiting a typical magnetization value of $\sim$3.1 $\mu_B$ [15]. However, there is no net moment on the Rh site. While in the $\alpha$-FM phase, both Fe moments ($\sim$3.2 $\mu_B$) and Rh moments ($\sim$0.9 $\mu_B$) are aligned ferromagnetically along the (001) direction [16].

In addition to the exotic properties related to the FM-AFM transition in the Fe-Rh alloys [17–19], the topological Hall effect (THE) has been observed recently in equiatomic Fe-Rh thin films [20]. In general, the THE is often considered as the hallmark of spin textures with a finite scalar spin chirality, e.g., magnetic skyrmions [21,22]. The THE in Fe-Rh film was proposed to be attributed to the emergence of noncollinear spin textures arising from the competition among different exchange interactions in its AFM state. The interfacial inhomogeneity in the magnetic thin film could lead to an inhomogeneous anomalous Hall effect (AHE), whose signal resembles the THE [23–26]. Considering that a large amount of the remaining FM phase persists in the AFM state of Fe-Rh film in the previous paper [20], the origin of THE requires further investigation. In addition, while most of the thin-film studies focus on equiatomic Fe-Rh films (i.e., $\sim$50% Fe content), less is known for Fe-Rh films with different Fe contents.

Here, we revisit the phase diagram of Fe-Rh epitaxial thin films by varying the Fe or Rh contents, and report a comprehensive study of their magnetic and transport properties by means of magnetization, electrical resistivity, and Hall resistivity measurements. Different from the bulk alloys, the Fe-Rh films show a pure $\alpha$ phase in a wide Fe concentration range (i.e., 33 to 53%). The absence of topological Hall resistivity in our high-quality epitaxial Fe-Rh films with different Fe contents excludes its possible nontrivial origin. We propose that the anomalous Hall resistivity caused by the remaining FM moments could give rise to a THE-like signal in the Hall resistivity.

## II. EXPERIMENTAL DETAILS

A series of $Fe_xRh_{100-x}$ ($30 \leqslant x \leqslant 57$) films with a thickness of $\sim$50 nm were epitaxially grown on (001)-oriented MgO substrates by magnetron cosputtering Fe and Rh targets in an ultrahigh vacuum chamber with a base pressure lower than $1 \times 10^{-8}$ Torr. To remove surface contamination, MgO substrates were preannealed at 600 °C for 1 h in the vacuum. Afterwards, the substrates were heated up to 700 °C, where both Fe and Rh atoms were deposited under a 3 mTorr-Ar pressure. During the deposition, MgO substrates were continuously rotated to improve homogeneity. After the deposition, $Fe_xRh_{100-x}$ films were annealed in situ at 750 °C for an extra hour to improve their crystallinity. Finally, a 3-nm-thick Ta cap layer was deposited at room temperature to avoid oxidation of $Fe_xRh_{100-x}$ films.

The crystal structure and the epitaxial nature of $Fe_xRh_{100-x}$ films were characterized by Bruker D8 Discover high-resolution x-ray diffractometer (HRXRD). The thickness of films were determined by x-ray reflectivity (XRR). The measurements of electrical resistivity ($\rho$), Hall resistivity ($\rho_{xy}$), and magnetization ($M$) were performed on a Quantum Design Physical Property Measurement System (PPMS) and a Magnetic Property Measurement System (MPMS), respectively. For the transport measurements, the $Fe_xRh_{100-x}$ films were patterned into a Hall-bar geometry (central area: 0.2 mm × 4 mm; electrodes: 0.4 mm × 0.65 mm) by using a shadow mask during the growth. To avoid spurious resistivity contributions due to misaligned Hall probes, the longitudinal contribution to the Hall resistivity was removed by an antisymmetrization procedure, i.e., $\rho_{xy}(H) = [\rho_{xy}(H) - \rho_{xy}(-H)]/2$. Similarly, in the case of longitudinal electrical resistivity measurements, the spurious transverse contribution was removed by a symmetrization procedure, i.e., $\rho(H) = [\rho(H) + \rho(-H)]/2$.

## III. RESULTS AND DISCUSSIONS

### A. X-ray diffraction and lattice parameters

We estimated the composition of $Fe_xRh_{100-x}$ films using the following model:

$$x = n \cdot N_A = (m/M_A) \cdot N_A = [(\beta \cdot v \cdot t \cdot S)/M_A] \cdot N_A. \quad (1)$$

Here, $n$, $m$, $N_A$, and $M_A$ are molar number, mass, Avogadro constant, and molar mass; $v$ and $t$ are deposition rate and time; $\beta$ and $S$ represent the density and surface area of the film, respectively. The deposition rate $v$ was controlled by adjusting the DC sputtering power of Fe and Rh targets, which was calibrated by the XRR measurements. Table I lists the sputtering power of Fe and Rh targets for different $Fe_xRh_{100-x}$ films. For instance, to produce the $Fe_{30}Rh_{70}$ film, the $P_{Fe}$ and $P_{Rh}$ were set to 20 and 15 W, respectively. We compared the magnetization and electrical resistivity results of the $Fe_{49}Rh_{51}$

TABLE I. Summary of the sputtering power of Fe ($P_{Fe}$) and Rh ($P_{Rh}$) targets for $Fe_xRh_{100-x}$ thin-film growth and the estimated Fe content for the deposited films. The deviation of Fe content is about 2%. Except $Fe_{30}Rh_{70}$ film, all other Fe-Rh films adopt a pure $\alpha$ phase.

| | | | | | | | |
|---|---|---|---|---|---|---|---|
| $P_{Fe}$ (W) | 20 | 25 | 30 | 35 | 40 | 45 | 35 |
| $P_{Rh}$ (W) | 15 | 15 | 15 | 15 | 15 | 15 | 10 |
| $x$ (Fe content) | 30 | 33 | 36 | 44 | 49 | 53 | 57 |

film prepared by cosputtering method with the one grown from $Fe_{50}Rh_{50}$ alloy target, both films show almost identical behaviors, suggesting that the above model gives correct Fe and Rh contents. Seven $Fe_xRh_{100-x}$ films with $x$ ranging from 30 to 57 were deposited.

The HRXRD measurements were performed to check the crystal structure and the epitaxial nature of the deposited $Fe_xRh_{100-x}$ films. Figure 2(a) shows representative XRD patterns for $Fe_xRh_{100-x}$ films with $x = 30$, 33, 49, and 57. For $x = 30$, the (002) reflection of $Fe_3Rh_7$ phase is clear, which adopts a $\gamma$ phase [28] and is consistent with the bulk phase diagram in Fig. 1. Since the $\gamma$-phase $Fe_{30}Rh_{70}$ is paramagnetic, its magnetic and electrical transport properties will not be discussed here. No sign of the $\alpha$ phase can be identified in this film. When increasing the Fe content up to 33%, the

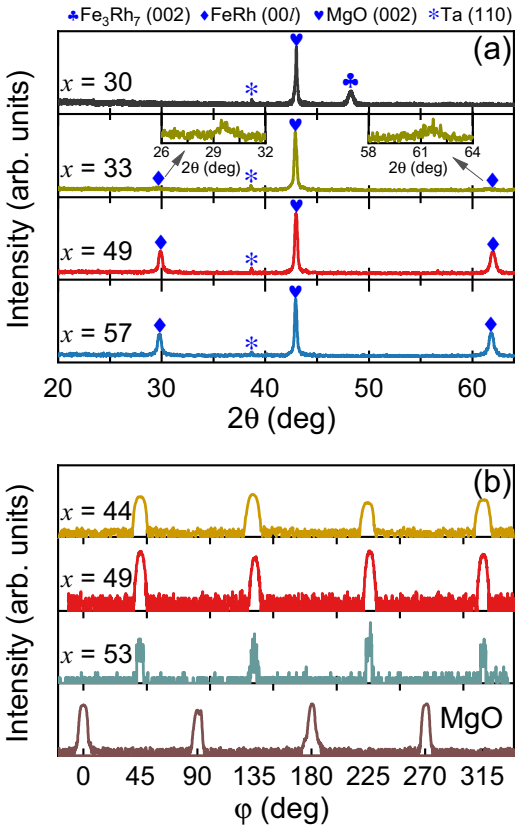


FIG. 2. (a) Representative XRD patterns of $Fe_xRh_{100-x}$ films for $x = 30$, 33, 49, and 57. The insets show enlarged plots of (001) and (002) reflections of $Fe_{33}Rh_{67}$ film. (b) $\varphi$-scan measurements for some selected $Fe_xRh_{100-x}$ films. The intensity is plotted on the logarithmic scale.

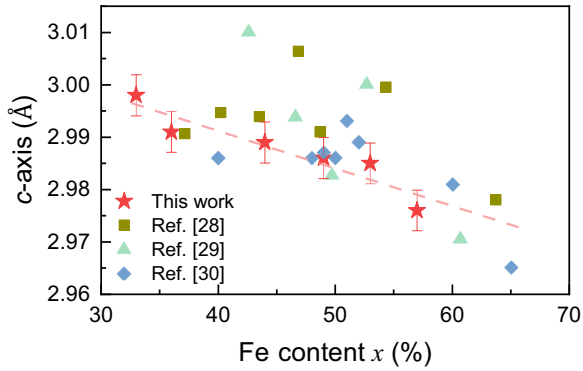


FIG. 3. Out-of-plane lattice parameters for the $Fe_xRh_{100-x}$ films and bulk counterparts as a function of the Fe content. The star symbols represent the current work, while the other symbols stand for the previous studies, which were taken from Refs. [28–30]. The dashed line is a guide to the eyes.

$\gamma$ phase disappears, in the meanwhile, $\alpha$ phase starts to show up [see insets in Fig. 2(a)]. For $33 \leqslant x \leqslant 57$, all $Fe_xRh_{100-x}$ films show a pure $\alpha$ phase, exhibiting distinct (001) and (002) reflections. This is obviously different from the bulk materials. In the bulk form, Fe-Rh alloys (with $x < 48$) show mixed $\gamma$ and $\alpha$ phases. The absence of foreign phases or misorientation suggests the good quality of our deposited $Fe_xRh_{100-x}$ films. It is noted that the $\alpha$-phase $Fe_xRh_{100-x}$ films were epitaxially grown on the MgO substrates with an in-plane 45° rotation, i.e., FeRh[110](001)—MgO[100](001) [5], which was further checked by $\varphi$-scan measurements [see Fig. 2(b)]. For $x = 33$, the intensities of the XRD reflections are rather low due to the increased mismatch between the film and the substrate, its epitaxial nature cannot be verified by the $\varphi$-scan measurements. For this film, the epitaxy is less good than the rest of the films, and it might be polycrystalline in nature but with preferred (00$l$) orientation.

We estimated the out-of-plane lattice constant (i.e., $c$ axis) for the $\alpha$-phase $Fe_xRh_{100-x}$ ($33 \leqslant x \leqslant 57$) films according to the XRD patterns. As shown in Fig. 3, for $x = 49$, the lattice parameter (2.989 Å) is almost identical to the value of $Fe_{50}Rh_{50}$ film (2.988 Å) grown by using a $Fe_{50}Rh_{50}$ alloy target [31], which further proves that the above model [see Eq. (1)] estimates the proper Fe or Rh concentration. The obtained lattice parameter linearly decreases as increases the Fe content $x$ (see star symbols), while in the previous studies, the lattice parameters are clearly more scattered (see square and triangle symbols). Such linear $x$-dependent lattice parameters again confirm that our $Fe_xRh_{100-x}$ films are very homogeneous and have a better quality.

### B. Magnetic properties of $Fe_xRh_{100-x}$ films

The $Fe_xRh_{100-x}$ ($33 \leqslant x \leqslant 57$) films were first characterized by temperature-dependent magnetization $M(T)$ and electrical resistivity $\rho(T)$. For the $\alpha$-phase $Fe_xRh_{100-x}$ ($33 \leqslant x \leqslant 53$) films, there is a clear anomaly around 380 K, which is attributed to the FM-AFM transition. Since the onset of this transition is above 400 K in zero-field condition in $Fe_xRh_{100-x}$ films, the entire transition can not be detected up to 400 K. However, the magnetic field can efficiently tune such a FM-

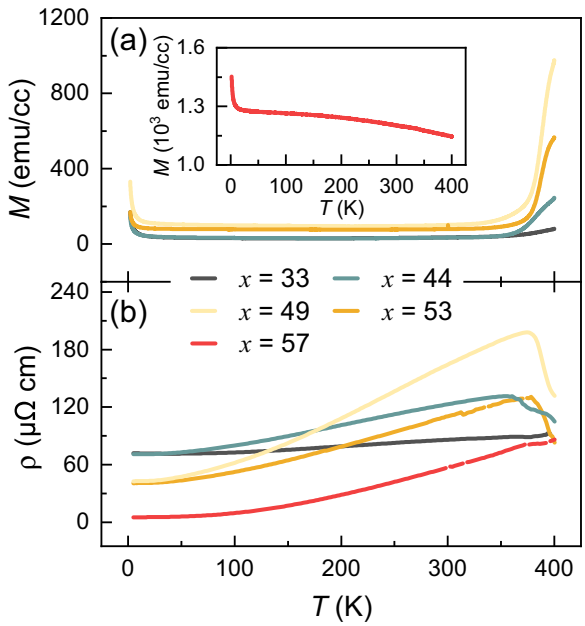


FIG. 4. Temperature-dependent magnetization collected in a field of $\mu_0 H = 0.1$ T (a) and zero-field electrical resistivity (b) for $Fe_xRh_{100-x}$ ($33 \leqslant x \leqslant 57$) films. The inset shows the magnetization data for $x = 57$ film.

AFM transition, and thus, the full transition can be clearly seen in a field of 5 T. For $x = 57$, the bulk sample undergoes a FM transition at very high temperature (~1000 K) (see Fig. 1). As shown in the inset of Fig. 4(a), the magnetization of $Fe_{57}Rh_{43}$ film resembles the pure Fe film [32], and there is no magnetic transition below 400 K. The magnetization of $Fe_{57}Rh_{43}$ film (~1200 emu/cc) is almost 10 times larger than the $Fe_xRh_{100-x}$ ($33 \leqslant x \leqslant 53$) films in their AFM state (~100 emu/cc). It is noted that in all the $Fe_xRh_{100-x}$ films, the upturn feature below 10 K is most likely attributed to the PM contribution of MgO substrate [33].

Figure 4(b) presents the zero-field temperature-dependent electrical resistivity $\rho(T)$ for $Fe_xRh_{100-x}$ ($33 \leqslant x \leqslant 57$) films. All the films show a typical metallic behavior below 350 K, the electrical resistivity decreases as lowering the temperature. Similar to the magnetization results, the resistivity jump at FM-AFM transition is not completed up to 400 K for $x = 44$, 49, 53. For $x = 33$, though the resistivity anomaly is very weak, it is still can be observed (see Fig. 5). While for $x = 57$, there is no clear anomaly in the studied temperature range, consisting with its magnetization data [see inset in Fig. 4(a)].

To better track the FM-AFM transition of $Fe_xRh_{100-x}$ films, the $M(T)$ and $\rho(T)$ were also collected upon heating and cooling the temperature in a field of $\mu_0 H = 5$ T. For $33 \leqslant x \leqslant 53$, the $M(T)$ exhibits a significant drop below 400 K upon cooling (see solid lines in the up panels in Fig. 5), indicating that these $Fe_xRh_{100-x}$ films undergo a magnetic phase transition from high-$T$ FM state to low-$T$ AFM state. Such a FM-AFM transition is clearly reflected also in the $\rho(T)$ data. As shown by solid lines in the bottom panels of Fig. 5, in contrast to the $M(T)$ data, the $\rho(T)$ undergoes a significant jump near the FM-AFM transition. In the FM state, both the Fe and Rh moments are aligned along the $c$ axis [16], resulting in a low-resistivity state. While in the AFM state, the enhanced magnetic scattering leads to a high-resistivity state. When increasing the magnetic field, the Rh and Fe moments are forced to ferromagnetically align again, accompanied by a resistivity drop at the metamagnetic transition [34]. Upon heating, all the $Fe_xRh_{100-x}$ films also undergo an AFM-FM transition, reflected by a jump in the magnetization or a drop in the electrical resistivity (see dashed lines in Fig. 5). While for $x = 57$ [see Fig. 5(f)], similar to the results in Fig. 4, no trace of magnetic transition can be identified in a field of 5 T, consistent with its FM nature in the studied temperature range.

Figures 6(a) and 6(b) plot the normalized temperature-dependent magnetization and electrical resistivity collected under various magnetic fields up to 5 T between 250 and 400 K for $Fe_{49}Rh_{51}$ film. When increasing the magnetic field, the FM-AFM (or AFM-FM) transition is suppressed to lower temperatures. As indicated by the arrows, the $T_t^{onset}$, $T_t^{mid}$, and $T_t^{offset}$ are defined as the onset, middle, and offset of the magnetic transition temperatures, respectively. We found that $T_t$ is suppressed at a rate of –7 K/T by the external magnetic field for $Fe_{49}Rh_{51}$ film. The $T_t(H)$ exhibits a linear field dependence up to 10 T [34]. To obtain zero-field magnetic transition temperatures, $T_t$ values determined from 5 T-data

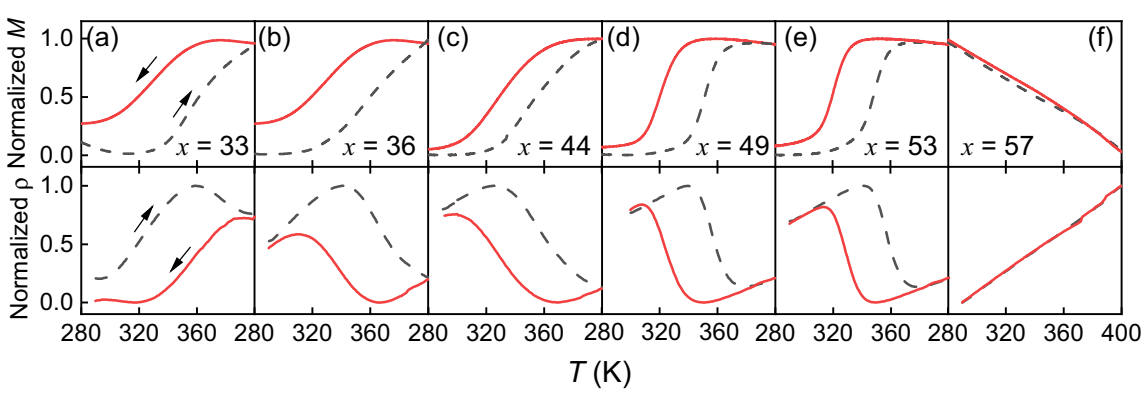


FIG. 5. Temperature dependence of the magnetization (top panels) and the electrical resistivity (bottom panels) for $Fe_xRh_{100-x}$ ($33 \leqslant x \leqslant 57$) films. All the data were collected in a magnetic field of $\mu_0 H = 5$ T during the cooling (solid lines) and heating processes (dashed lines).To better compare the results of different films, both the magnetization and electrical resistivity data are normalized to the values between 0 and 1.

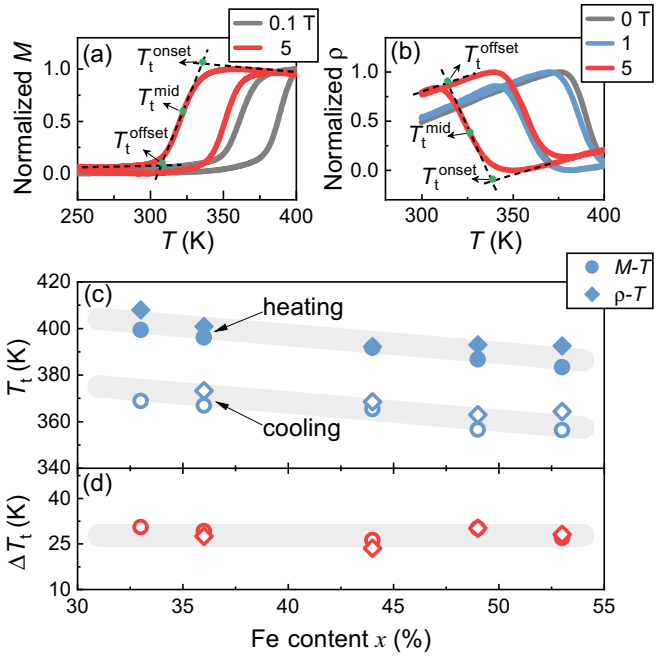


FIG. 6. Temperature-dependent magnetization (a) and electrical resistivity (b) collected under various magnetic fields up to 5 T for $Fe_{49}Rh_{51}$ film. Both the magnetization and electrical resistivity data are normalized to the values between 0 and 1. (c) The magnetic transition temperatures $T_t$ (i.e., $T_t^{mid}$) determined from magnetization and electrical resistivity measurements vs Fe content. Open and solid symbols represent the $T_t$ determined from the measurements upon cooling and heating processes, respectively. (d) The transition width $\Delta T_t$ (= $T_t^{onset}$ - $T_t^{offset}$) of the FM-AFM (or AFM-FM) transition vs the Fe content.

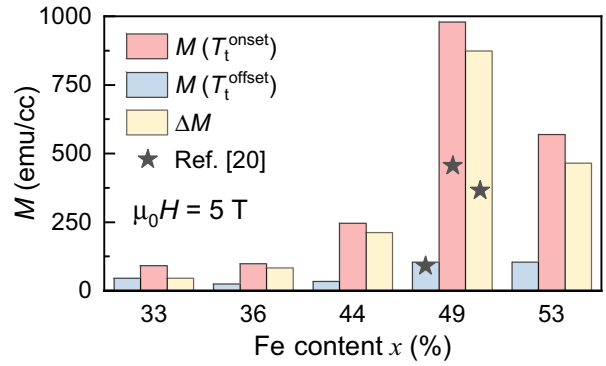


FIG. 7. The magnetization at $T_t^{onset}$ and $T_t^{offset}$, and their difference $\Delta M$ [= $M(T_t^{onset})$ - $M(T_t^{offset})$] for various $Fe_xRh_{100-x}$ films ($33 \leqslant x \leqslant 53$). The data were obtained from the magnetization collected during the cooling process (see details in Fig. 5). For the magnetization at $T_t^{onset}$ and $T_t^{offset}$, the background signal from the MgO substrates was subtracted according to $M_{FeRh}(T_t^{onset}) = M_{raw}(T_t^{onset})$ - $M_{MgO}(T_t^{onset})$. The data extracted from Ref. [20] were also presented.

(see Fig. 5) were extrapolated to zero field using the above rate. The estimated zero-field $T_t$ values (here we choose $T_t^{mid}$) are summarized in Fig. 6(c) as a function of Fe content. The $T_t$ determined from magnetization and electrical resistivity measurements are highly consistent. When increasing the Fe content, $T_t$ determined during the heating process slightly decreases from 400 K for $x = 33$ to 385 K for $x = 53$. The $T_t$ determined during the cooling process exhibits an almost identical trend, yielding a $x$-independent transition width $\Delta T_t$ [see Fig. 6(d)]. Such a $\Delta T_t(x)$ indicates that the first-order FM-AFM transition exists in the $Fe_xRh_{100-x}$ ($33 \leqslant x \leqslant 53$) films with a much wider Fe content than the bulk alloys. For the latter case, it is limited only at $48 \leqslant x \leqslant 54$ (see details in Fig. 1).

To quantitatively describe the FM-AFM transition in $Fe_xRh_{100-x}$ ($33 \leqslant x \leqslant 53$) films, their magnetization at different magnetic states are summarized in Fig. 7. The $M(T_t^{onset})$ represents the magnetization at $T_t^{onset}$ (i.e., FM state), while $M(T_t^{offset})$ is the magnetization at $T_t^{offset}$ (i.e., AFM state). Both $M(T_t^{onset})$ and $M(T_t^{offset})$ reach a maximum value as the Fe content increases up to 49%. According to the XRD results [see Fig. 2(a)], all the $Fe_xRh_{100-x}$ ($33 \leqslant x \leqslant 53$) films show a pure $\alpha$ phase at room temperature, which is completely different from the bulk alloys (see Fig. 1). Therefore, in the $Fe_xRh_{100-x}$ films, the larger magnetization value indicates a larger FM phase concentration at $T \geqslant T_t^{onset}$, and vice versa. As can be clearly seen in Fig. 7, the magnetization of $x = 49$ and 53 films is significantly larger than that of $x < 49$, implying that most of the Fe moments stay PM in the latter cases. In the AFM state (i.e., $T \leqslant T_t^{offset}$), the magnetization is mainly attributed to the pinned Fe moments at the $Ta/Fe_xRh_{100-x}$ or $Fe_xRh_{100-x}/MgO$ interfaces [35,36]. As a consequence, the smaller magnetization value indicates a larger AFM phase concentration at $T \leqslant T_t^{offset}$, and vice versa. We also summarized the magnetization drop $\Delta M$, a measure of the FM-AFM transition, versus the Fe content in Fig. 6. Similar to the $M(T_t^{onset})$, the $\Delta M$ also reaches a maximum value at $x = 49$, which is significantly larger than the rest of $Fe_xRh_{100-x}$ films.

For the Fe-Rh-based spintronic applications, the $Fe_xRh_{100-x}$ films with a large $\Delta M$ value are preferred [12–14], since it could also give rise to a more pronounced jump in the electrical resistivity. The estimated resistivity jumps $\Delta\rho$ [$= \rho(T_t^{offset}) - \rho(T_t^{onset})$] [see details in Fig. 6(b)] of $Fe_xRh_{100-x}$ ($33 \leqslant x \leqslant 53$) films are summarized in the phase diagram (see Fig. 1). Indeed, for $x = 49$ and 53, the $\Delta\rho$ values are significantly larger than that of $x < 49$. For instance, the $\Delta\rho = 55$ μΩ cm for $x = 49$, while it is less than 10 μΩ cm for $x = 33$. Our results demonstrate that the $Fe_xRh_{100-x}$ films with Fe content up to 53% exhibit magnetic and transport properties that are comparable to the ideal 49% case. While for $x \leqslant 44$, the FM-AFM transition is less pronounced, leading to small $\Delta M$ and $\Delta\rho$ values.

### C. Magnetoresistivity and Hall resistivity

The field-dependent longitudinal and transverse resistivity were measured in a wide-temperature range for $Fe_xRh_{100-x}$ films. Since the films with $x = 44$, 49, and 53 exhibit a more pronounced magnetic phase transition, here, the field-dependent measurements were focused on these films. Figures 8(a)–8(c) plot the magnetoresistivity (MR) collected at various temperatures with the magnetic field up to 9 T. The MR values of $Fe_xRh_{100-x}$ films at $\mu_0 H = 9$ T are

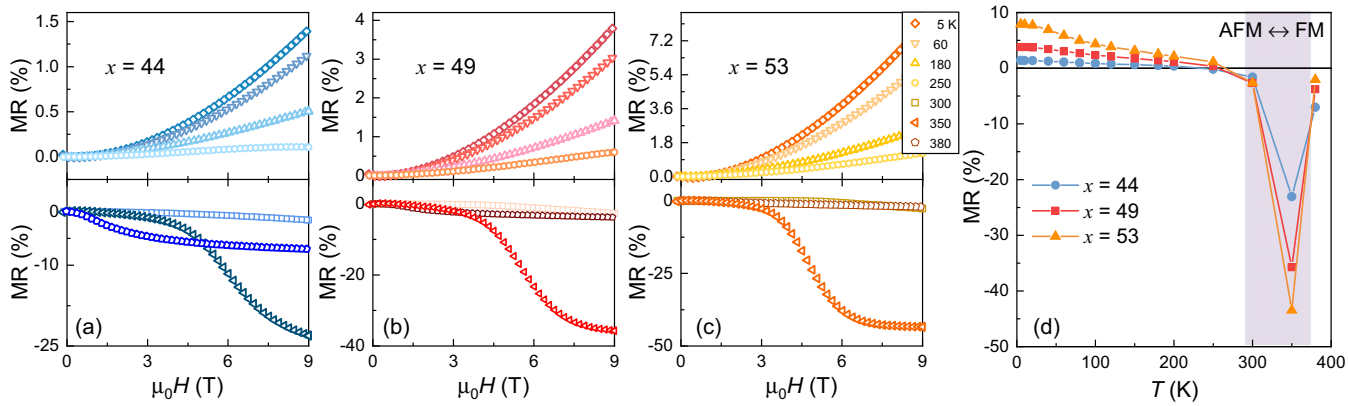


FIG. 8. Magnetoresistivity up to 9 T for (a) $x = 44$, (b) $x = 49$, and (c) $x = 53$ collected at various temperatures covering both the FM- and AFM states. (d) Temperature-dependent 9-T MR values for the above three films. The magnetic field was applied along the out-of-plane direction. The MR was calculated following $\mathrm{MR} = [\rho(H) - \rho(0)]/\rho(0)$, where $\rho(0)$ is the zero-field electrical resistivity. The shaded region highlights the coexistence of AFM and FM phases, where a giant MR appears.

summarized in Fig. 8(d). All three films exhibit similar temperature-dependent MR in the studied temperature range. In the AFM state ($T \leqslant 250$ K), the MR is positive, which is mainly attributed to the enhanced magnetic scattering by applying external magnetic field. Once the magnetic field destroys the AFM state and fully polarizes the Fe moments, the MR exhibits a significant drop near the metamagnetic transition [34,37]. As the temperature increases close to room temperature, where the FM phase shows up, the MR becomes negative, a typical feature for the ferromagnets. While in the mixed AFM and FM states, a giant MR was observed, whose value reaching almost 50% at $T = 350$ K for $x = 53$. Such a giant MR is related to the field-induced metamagnetic transition in $Fe_xRh_{100-x}$ films, as observed in their AFM state [37].

The $Fe_{50}Rh_{50}$ film has been found to exhibit a topological Hall effect in a wide-temperature range [20], which is often attributed to the topological spin textures in magnetic materials [38,39]. Since the Fe-Rh alloys exhibit a simple G-type AFM structure, the appearance of THE is rather puzzling. To further investigate the possible THE in $Fe_xRh_{100-x}$ films, we also performed systematic Hall resistivity measurements. As shown in Fig. 9, the $\rho_{xy}(H)$ were collected at various temperatures covering both the AFM and FM states of $Fe_xRh_{100-x}$ ($x = 44$, 49, and 53) films. In the FM state, the $\rho_{xy}(H)$ is dominated by the anomalous Hall effect (see 380-K curves in Fig. 9). While in the AFM state (i.e., $T < 300$ K), in contrast to the previous paper [20], all the $\rho_{xy}(H)$ curves exhibit almost a linear-field dependence at $\mu_0 H \leqslant 6$ T, definitely excluding the possible THE in our $Fe_xRh_{100-x}$ films. While for $\mu_0 H > 6$ T, the $\rho_{xy}$ becomes nonlinear, which is clearly reflected by the 300-K curves in Fig. 9. Such a nonlinear $\rho_{xy}(H)$ is attributed to the field-induced metamagnetic transition in $Fe_xRh_{100-x}$ films. The metamagnetic transition field is about 8.3 T at 300 K, which increases when decreasing temperature, reaching 9.8 T at $T = 291$ K [34]. Therefore, the $\rho_{xy}$ is always dominated by the ordinary Hall effect (OHE) at $\mu_0 H \leqslant 9$ T for $T < 250$ K. However, once the magnetic field is larger than the metamagnetic transition field, the $\rho_{xy}(H)$ resembles the typical features of AHE in ferromagnets. Interestingly, in the mixed AFM and FM states, our $Fe_xRh_{100-x}$ films exhibit a clear hump-like anomaly in the $\rho_{xy}(H)$. As shown in Fig. 9, a clear hump can be observed at $\mu_0 H \sim 3$ T at 350 K. Such a hump-like anomaly resembles the topological Hall resistivity reported in the previous paper [20]. However, such an anomaly is absent in the AFM state, implying that its origin is very unlikely the noncollinear spin textures. On the contrary, this anomaly can be reproduced, assuming anomalous Hall resistivity with different origins existing in the $Fe_xRh_{100-x}$ films (see details in the Discussion section).

### D. Discussion

First, we discuss the magnetic phase diagram of $Fe_xRh_{100-x}$ films. After optimizing the growth conditions, we could produce phase-pure $Fe_xRh_{100-x}$ films with a wide $x$ range (i.e., Fe content). For the bulk case, the $Fe_xRh_{100-x}$ alloys adopt the mixed $\alpha$ and $\gamma$ phases for $33 \leqslant x \leqslant 48$ [see details in Fig. 1(a)]. While the $\gamma$ phase remains PM, the $\alpha$

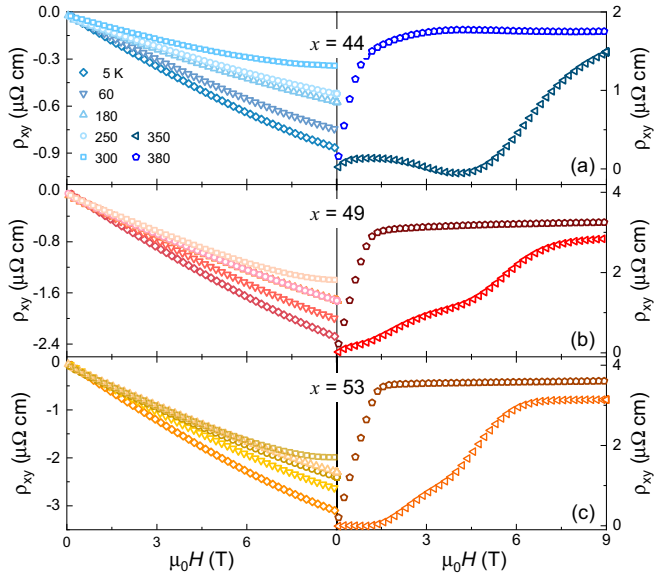


FIG. 9. Field-dependent Hall resistivity $\rho_{xy}(H)$ collected at various temperature below 400 K up to 9 T for $Fe_xRh_{100-x}$ films with (a) $x = 44$, (b) $x = 49$, and (c) $x = 53$.

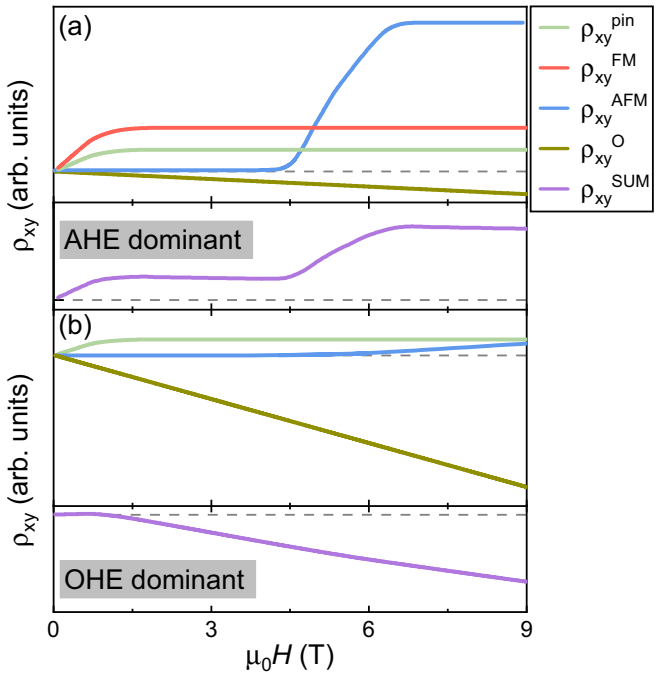


FIG. 10. Schematic plots of different contributions to the Hall resistivity for the $Fe_xRh_{100-x}$ films in the mixed AFM and FM states (a) or in the AFM state (b). In the mixed FM and AFM states, $\rho_{xy}^{SUM} = \rho_{xy}^{O} + \rho_{xy}^{pin} + \rho_{xy}^{FM} + \rho_{xy}^{AFM}$, while in the AFM state, $\rho_{xy}^{SUM} = \rho_{xy}^{O} + \rho_{xy}^{pin} + \rho_{xy}^{AFM}$. Here, $\rho_{xy}^{pin}$, $\rho_{xy}^{AFM}$, and $\rho_{xy}^{FM}$ all denote the anomalous Hall resistivity.

phase becomes FM below certain temperatures. For $x > 48$, the $Fe_xRh_{100-x}$ alloys show a pure $\alpha$ phase with the Curie temperatures between 600 and 1000 K. For some particular Fe concentrations, i.e., $48 \leqslant x \leqslant 54$, the $Fe_xRh_{100-x}$ alloys undergo multiple magnetic transitions, from PM state to the FM state, and then finally to the AFM state. Different from the bulk alloys, $Fe_xRh_{100-x}$ films show significantly different structural and magnetic properties. For the Fe-deficient case, $Fe_{30}Rh_{70}$ film adopts a $\gamma$ phase, and there is no magnetic transition below 400 K, implying its PM nature. For $33 \leqslant x \leqslant 57$, all $Fe_xRh_{100-x}$ films show a pure $\alpha$ phase. For the bulk alloys, no additional magnetic transition has been found below the Curie temperature for $33 \leqslant x \leqslant 48$. While in the case of films, there is a distinct FM-AFM transition for $33 \leqslant x \leqslant 53$, whose critical temperature $T_t$ determined during the heating process slightly decreases from 400 K for $x = 33$ to 385 K for $x = 53$ [marked as $\alpha$-(AFM+PM) in Fig. 1(a)]. In the case of Fe-rich films (i.e., $x \geqslant 57$), although they show a pure $\alpha$ phase, the FM-AFM transition is absent, and all the films host a FM ground state. It is noted that the FM-AFM transition exists in the $Fe_xRh_{100-x}$ films with a wide Fe content; however, there is a large portion of remaining PM phase for $x \leqslant 44$, which is reflected by a reduced resistivity jump $\Delta\rho$ and a magnetization drop $\Delta M$ (see details in Fig. 1 and Fig. 7). In addition, in all the $Fe_xRh_{100-x}$ films, the Fe moments pinned at the interfaces also contribute to the magnetization in the AFM state and could lead to a hump-like anomaly in the Hall resistivity. The absence of AHE in the AFM state proves that our $Fe_xRh_{100-x}$ films have negligible remaining FM contribution (see Fig. 9).

Now we discuss the possible THE in $Fe_xRh_{100-x}$ films. Based on the experimental observations in Fig. 9, we show the schematic plots in Fig. 10 to discuss the Hall resistivity in $Fe_xRh_{100-x}$ films. The linear $\rho_{xy}(H)$ is caused by the OHE (marked as $\rho_{xy}^{O}$), whose negative slope suggests that the electron carriers are dominant in the $Fe_xRh_{100-x}$ films. The $\rho_{xy}^{pin}$, $\rho_{xy}^{AFM}$, and $\rho_{xy}^{FM}$ all denote the anomalous Hall resistivity, which are attributed to the ferromagnetically pinned Fe moments at the interfaces, AFM magnetization, and FM magnetization, respectively. In general, both $\rho_{xy}^{pin}$ and $\rho_{xy}^{FM}$ are proportional to the magnetization (i.e., $\rho_{xy}^{pin} \propto M^{pin}$, $\rho_{xy}^{FM} \propto M^{FM}$), typical for ferromagnets [40]. Here, $M^{pin}$ and $M^{FM}$ are the magnetization attributed to the pinned Fe moments at the interfaces and the FM regions of the films, both of which saturate when increasing the magnetic field up to 1 T. While the $\rho_{xy}^{AFM}$ is proportional to $\rho^2 M$, $\rho M$, or their combinations, depending on the intrinsic or extrinsic mechanism [41]. Here we use $\rho M$ to produce $\rho_{xy}^{AFM}$, while the $\rho^2 M$ leads to similar behaviors. We assume that the AFM magnetization $M^{AFM}$ is linear in the low-field region but undergoes a metamagnetic transition at higher magnetic field, whose critical field increases as lowering the temperature. For example, the metamagnetic transition field is close to 5 T near room temperature but increases to 7.5 T at 290 K [34]. As shown in Fig. 10(a), in the mixed AFM and FM states, the AHE due to FM and AFM magnetization (i.e., $\rho_{xy}^{FM}$ and $\rho_{xy}^{AFM}$) is dominant, and as a consequence, the total Hall resistivity $\rho_{xy}^{SUM}$ shows a step-like feature, typical for the magnets that undergo a metamagentic transition. The $\rho_{xy}^{SUM}$ qualitatively agrees very well with $\rho_{xy}(H)$ collected at 350 K for $Fe_xRh_{100-x}$ films (see details in Fig. 9). In the AFM state, as shown in Fig. 10(b), since the OHE is dominant, the observed $\rho_{xy}(H)$ is almost linear in field. While the $\rho_{xy}^{pin}$ could cause a hump-like anomaly in the $\rho_{xy}^{SUM}$, resembling the observed topological Hall resistivity in Ref. [20]. However, such an anomaly is clearly absent in our $Fe_xRh_{100-x}$ films with different Fe contents (see Fig. 9). Since the $\rho_{xy}^{pin}$ is attributed to the FM Fe moments pinned at the interfaces, such a hump-like anomaly in the $\rho_{xy}(H)$ should strongly depend on the thin-film quality. We summarized the magnetization values from Ref. [20] in Fig. 7 to compare with our films. Although the remaining magnetization $M(T_t^{offset})$ is comparable to our $Fe_{49}Rh_{51}$ film, the FM-state magnetization $M(T_t^{onset})$ is two times smaller than our film. As a consequence, the $\rho_{xy}(H)$ is significantly affected by the $\rho_{xy}^{pin}$ in the previous paper. In addition, since the $\rho_{xy}^{pin}$ has an opposite sign against the $\rho_{xy}^{O}$, the large contribution of $\rho_{xy}^{pin}$ might cause a sign change in the $\rho_{xy}(H)$ when cooling the film down to lower temperatures. Indeed, such a sign change was observed in the previous paper, the slope of $\rho_{xy}(H)$ becomes positive below 80 K [20]. While in our $Fe_xRh_{100-x}$ ($x = 44$, 49, and 53) films, the $\rho_{xy}(H)$ is always negative in the AFM state, which again proves that the remaining FM magnetization at the interfaces has little effect in our $Fe_xRh_{100-x}$ films. To conclude, the observed THE in $Fe_xRh_{100-x}$ films is most likely an extrinsic effect. The other techniques, such as resonant x-ray scattering or Lorentz transmission electron microscopy, are highly desirable to search for possible topological magnetic phases in $Fe_xRh_{100-x}$ family.

## IV. CONCLUSIONS

To summarize, we grew a series of epitaxial $Fe_xRh_{100-x}$ ($30 \leqslant x \leqslant 57$) films on MgO substrates. By systematic x-ray diffraction, magnetization, and electrical resistivity measurements, we established the structural and magnetic phase diagram of $Fe_xRh_{100-x}$ films. For $x \leqslant 30$, $Fe_xRh_{100-x}$ films are PM and adopt a $\gamma$ phase. For $x \geqslant 33$, all films show a pure $\alpha$ phase. In the bulk $Fe_xRh_{100-x}$ alloys, the FM-AFM transition is limited only at $48 \leqslant x \leqslant 54$. While the FM-AFM transition persists in the $Fe_xRh_{100-x}$ films with $33 \leqslant x \leqslant 53$, and the transition temperature slightly decreases from 400 K for $x = 33$ to 385 K for $x = 53$. As further increases the Fe content (i.e., $x > 53$), the FM-AFM transition no longer exists, and $Fe_xRh_{100-x}$ films are FM in the studied temperature range. The resistivity jump and magnetization drop at the FM-AFM transition are much more pronounced in the $Fe_xRh_{100-x}$ films with ~50% Fe content than in the Fe-deficient films, the latter have a large amount of PM phase. The magnetoresistivity is positive and weak in the AFM state, while it becomes negative when the FM phase shows up, and a giant MR appears in the mixed AFM- and FM states. The Hall resistivity measurements reveal trivial behaviors in the $Fe_xRh_{100-x}$ films, which is dominated by the OHE in the AFM state and by the AHE in the mixed or FM state, respectively. Our results demonstrate that the previously observed topological Hall resistivity is absent in our $Fe_xRh_{100-x}$ ($x = 44$, 49, and 53) films. We proposed that the AHE caused by the FM Fe moments at the interfaces could explain the hump-like anomaly in the Hall resistivity. To conclude, the observed THE in $Fe_xRh_{100-x}$ films can be explained by extrinsic mechanisms rather than the presence of noncollinear spin textures.

## ACKNOWLEDGMENTS

The authors thank G. T. Lin and J. Ma for their assistance during the transport measurements. This work was supported by the Natural Science Foundation of Shanghai (Grants No. 21ZR1420500 and No. 21JC1402300), Natural Science Foundation of Chongqing (Grant No. 2022NSCQ-MSX1468), the National Natural Science Foundation of China (Grants No. 12174103 and No. 12374105). Y.X. acknowledges support from the Shanghai Pujiang Program (Grant No. 21PJ1403100).

[1] V. Uhlíř, J. A. Arregi, and E. E. Fullerton, Colossal magnetic phase transition asymmetry in mesoscale FeRh stripes, Nat. Commun. **7**, 13113 (2016).

[2] G. Li, R. Medapalli, J. H. Mentink, R. V. Mikhaylovskiy, T. G. H. Blank, S. K. K. Patel, A. K. Zvezdin, T. Rasing, E. E. Fullerton, and A. V. Kimel, Ultrafast kinetics of the antiferromagnetic-ferromagnetic phase transition in FeRh, Nat. Commun. **13**, 2998 (2022).

[3] C. J. Kinane, M. Loving, M. A. d. Vries, R. Fan, T. R. Charlton, J. S. Claydon, D. A. Arena, F. Maccherozzi, S. S. Dhesi, D. Heiman *et al.*, Observation of a temperature dependent asymmetry in the domain structure of a Pd-doped FeRh epilayer, New J. Phys. **16**, 113073 (2014).

[4] J. A. Arregi, O. C. V. Caha, and V. C. V. Uhlíř, Evolution of strain across the magnetostructural phase transition in epitaxial FeRh films on different substrates, Phys. Rev. B **101**, 174413 (2020).

[5] Y. Xie, Q. Zhan, T. Shang, H. Yang, B. Wang, J. Tang, and R.-W. Li, Effect of epitaxial strain and lattice mismatch on magnetic and transport behaviors in metamagnetic FeRh thin films, AIP Adv. **7**, 056314 (2017).

[6] K. Qiao, F. Hu, Y. Liu, J. Li, H. Kuang, H. Zhang, W. Liang, J. Wang, J. Sun, and B. Shen, Novel reduction of hysteresis loss controlled by strain memory effect in FeRh/PMN-PT heterostructures, Nano Energy **59**, 285 (2019).

[7] R. O. Cherifi, V. Ivanovskaya, L. C. Phillips, A. Zobelli, I. C. Infante, E. Jacquet, V. Garcia, S. Fusil, P. R. Briddon, N. Guiblin *et al.*, Electric-field control of magnetic order above room temperature, Nat. Mater. **13**, 345 (2014).

[8] S. Maat, J.-U. Thiele, and E. E. Fullerton, Temperature and field hysteresis of the antiferromagnetic-to-ferromagnetic phase transition in epitaxial FeRh films, Phys. Rev. B **72**, 214432 (2005).

[9] Y. Lee, Z. Q. Liu, J. T. Heron, J. D. Clarkson, J. Hong, C. Ko, M. D. Biegalski, U. Aschauer, S. L. Hsu *et al.*, Large resistivity modulation in mixed-phase metallic systems, Nat. Commun. **6**, 5959 (2015).

[10] Z. Q. Liu, L. Li, Z. Gai, J. D. Clarkson, S. L. Hsu, A. T. Wong, L. S. Fan, M.-W. Lin, C. M. Rouleau, T. Z. Ward, H. N. Lee, A. S. Sefat, H. M. Christen, and R. Ramesh, Full electroresistance modulation in a mixed-phase metallic alloy, Phys. Rev. Lett. **116**, 097203 (2016).

[11] C. Cao, S. Chen, B. Cui, G. Yu, C. Jiang, Z. Yang, X. Qiu, T. Shang, Y. Xu, and Q. Zhan, Efficient tuning of the spin–orbit torque via the magnetic phase transition of FeRh, ACS Nano **16**, 12727 (2022).

[12] K. Qiao, J. Wang, F. Hu, J. Li, C. Zhang, Y. Liu, Z. Yu, Y. Gao, J. Su, F. Shen *et al.*, Regulation of phase transition and magnetocaloric effect by ferroelectric domains in FeRh/PMN-PT heterojunctions, Acta Mater. **191**, 51 (2020).

[13] X. Marti, I. Fina, C. Frontera, J. Liu, P. Wadley, Q. He, R. J. Paull, J. D. Clarkson, J. Kudrnovský, I. Turek *et al.*, Room-temperature antiferromagnetic memory resistor, Nat. Mater. **13**, 367 (2014).

[14] J.-U. Thiele, S. Maat, J. L. Robertson, and E. E. Fullerton, Magnetic and structural properties of FePt–FeRh exchange spring films for thermally assisted magnetic recording media, IEEE Trans. Magn. **40**, 2537 (2004).

[15] E. F. Bertaut, A. Delapalme, F. Forrat, G. Roult, F. De Bergevin, and R. Pauthenet, Magnetic structure work at the Nuclear Center of Grenoble, J. Appl. Phys. **33**, 1123 (1962).

[16] G. Shirane, C. W. Chen, P. A. Flinn, and R. Nathans, Hyperfine fields and magnetic moments in the Fe-Rh system, J. Appl. Phys. **34**, 1044 (1963).

[17] X. Zhu, Y. Xu, C. Cao, T. Shang, Y. Xie, and Q. Zhan, Recent developments on the magnetic and electrical transport properties of FeRh- and Rh-based heterostructures, J. Phys.: Condens. Matter **34**, 144004 (2022).

[18] X. Zhu, Y. Li, Y. Xie, Q. Qiu, C. Cao, X. Hu, W. Xie, T. Shang, Y. Xu, L. Sun *et al.*, Magnetocrystalline anisotropy of epitaxially grown FeRh/MgO(001) films, J. Alloys Compd. **917**, 165566 (2022).

[19] Y. Liu, L. C. Phillips, R. Mattana, M. Bibes, A. Barthélémy, and B. Dkhil, Large reversible caloric effect in FeRh thin films via a dual-stimulus multicaloric cycle, Nat. Commun. **7**, 11614 (2016).

[20] S. Zhang, S. Xia, Q. Cao, D. Wang, R. Liu, and Y. Du, Observation of topological Hall effect in antiferromagnetic FeRh film, Appl. Phys. Lett. **115**, 022404 (2019).

[21] J. Matsuno, N. Ogawa, K. Yasuda, F. Kagawa, W. Koshibae, N. Nagaosa, Y. Tokura, and M. Kawasaki, Interface-driven topological Hall effect in $SrRuO_3$-$SrIrO_3$ bilayer, Sci. Adv. **2**, e1600304 (2016).

[22] A. Neubauer, C. Pfleiderer, B. Binz, A. Rosch, R. Ritz, P. G. Niklowitz, and P. Böni, Topological Hall effect in the *a* phase of MnSi, Phys. Rev. Lett. **102**, 186602 (2009).

[23] G. Kimbell, C. Kim, W. Wu, M. Cuoco, and J. W. A. Robinson, Challenges in identifying chiral spin textures via the topological Hall effect, Commun. Mater. **3**, 19 (2022).

[24] D. J. Groenendijk, C. Autieri, T. C. van Thiel, W. Brzezicki, J. R. Hortensius, D. Afanasiev, N. Gauquelin, P. Barone, K. H. W. van den Bos, S. van Aert, J. Verbeeck, A. Filippetti, S. Picozzi, M. Cuoco, and A. D. Caviglia, Berry phase engineering at oxide interfaces, Phys. Rev. Res. **2**, 023404 (2020).

[25] L. Wang, Q. Feng, H. G. Lee, E. K. Ko, Q. Lu, and T. W. Noh, Controllable thickness inhomogeneity and Berry curvature engineering of anomalous Hall effect in $SrRuO_3$ ultrathin films, Nano Lett. **20**, 2468 (2020).

[26] Y. Zhang and S. Granville, Two-channel anomalous hall effect originating from the intermixing in $Mn_2CoAl$/Pd thin films, Phys. Rev. B **106**, 144414 (2022).

[27] O. K. Goldbeck, *IRON-Binary Phase Diagrams* (Springer, Berlin, 1982)

[28] S. Inoue, H. Yu Yu Ko, and T. Suzuki, Magnetic properties of single-crystalline FeRh alloy thin films, IEEE Trans. Magn. **44**, 2875 (2008).

[29] A. B. Mei, Y. Tang, J. L. Grab, J. Schubert, D. C. Ralph, and D. G. Schlom, Structural, magnetic, and transport properties of $Fe_{1-x}Rh_x$/MgO(001) films grown by molecular-beam epitaxy, Appl. Phys. Lett. **113**, 082403 (2018).

[30] G. Shirane, C. W. Chen, P. A. Flinn, and R. Nathans, Mössbauer study of hyperfine fields and isomer shifts in the Fe-Rh alloys, Phys. Rev. **131**, 183 (1963).

[31] Y. Xie, Q. Zhan, Y. Hu, X. Hu, X. Chi, C. Zhang, H. Yang, W. Xie, X. Zhu, J. Gao *et al.*, Magnetocrystalline anisotropy imprinting of an antiferromagnet on an amorphous ferromagnet in FeRh/CoFeB heterostructures, NPG Asia Mater. **12**, 67 (2020).

[32] L. Bergqvist and A. Bergman, Realistic finite temperature simulations of magnetic systems using quantum statistics, Phys. Rev. Mater. **2**, 013802 (2018).

[33] R. Cabassi, F. Bolzoni, and F. Casoli, Differential method for sample holder background subtraction in superconducting quantum interference device (SQUID) magnetometry, Meas. Sci. Technol. **21**, 035701 (2010).

[34] M. A. d. Vries, M. Loving, A. P. Mihai, L. H. Lewis, D. Heiman, and C. H. Marrows, Hall-effect characterization of the metamagnetic transition in FeRh, New J. Phys. **15**, 013008 (2013).

[35] R. Fan, C. J. Kinane, T. R. Charlton, R. Dorner, M. Ali, M. A. de Vries, R. M. D. Brydson, C. H. Marrows, B. J. Hickey, D. A. Arena, B. K. Tanner, G. Nisbet, and S. Langridge, Ferromagnetism at the interfaces of antiferromagnetic FeRh epilayers, Phys. Rev. B **82**, 184418 (2010).

[36] M. Loving, F. Jimenez-Villacorta, B. Kaeswurm, D. A. Arena, C. H. Marrows, and L. H. Lewis, Structural evidence for stabilized ferromagnetism in epitaxial FeRh nanoislands, J. Phys. D: Appl. Phys. **46**, 162002 (2013).

[37] I. Suzuki, T. Naito, M. Itoh, T. Sato, and T. Taniyama, Clear correspondence between magnetoresistance and magnetization of epitaxially grown ordered FeRh thin films, J. Appl. Phys. **109**, 07C717 (2011).

[38] M. Raju, A. Yagil, A. Soumyanarayanan, A. K. C. Tan, A. Almoalem, F. Ma, O. M. Auslaender, and C. Panagopoulos, The evolution of skyrmions in Ir/Fe/Co/Pt multilayers and their topological Hall signature, Nat. Commun. **10**, 696 (2019).

[39] A. Zadorozhnyi and Y. Dahnovsky, Topological hall effect in three-dimensional centrosymmetric magnetic skyrmion crystals, Phys. Rev. B **107**, 054436 (2023).

[40] R. Karplus and J. M. Luttinger, Hall effect in ferromagnetics, Phys. Rev. **95**, 1154 (1954).

[41] N. Nagaosa, J. Sinova, S. Onoda, A. H. MacDonald, and N. P. Ong, Anomalous Hall effect, Rev. Mod. Phys. **82**, 1539 (2010).